

# ANODIC OXIDES ON SILICON

H. J. LEWERENZ

Hahn-Meitner-Institut Berlin, Bereich Photochemische Energiewandlung, Postfach 39 01 28, 1000 Berlin 39, Germany

(Received 16 September 1991)

**Abstract**—The formation of anodic oxides on n- and p-type silicon is investigated by chronoamperometry, *in situ* ellipsometry, *in situ* excess microwave reflectivity measurements, *ex situ* X-ray and ultraviolet photoelectron spectroscopy (XPS and UPS) and low energy electron diffraction (LEED). Comparison with data on thermally oxidized samples reveals that anodic oxides are less dense being characterized by a composition profile. In addition differences in the etching rate and composition profile of anodic oxides on n-Si and p-Si are observed. The microwave measurements allow a correlation between oxide formation in  $\text{NH}_4\text{F}$  solution and changes in charge transfer velocity and surface recombination velocity. At high anodic potentials, photocurrent oscillations on oxidized samples occur at oxide coverages of about 35–40 Å as evidenced by XPS. The surface conditions during dark current flow are investigated by XPS, UPS and LEED. The dark current is associated with distinct surface changes resulting in an electrolytically hydrogenated surface if samples are emersed after the dark current decay. Photocurrent multiplication processes are briefly described, studied by intensity modulated photocurrent spectroscopy (IMPS).

**Key words:** silicon, interface analysis, photoelectrochemistry, oxides.

## 1. INTRODUCTION

The study of silicon-solution interfaces has found renewed interest in recent years. The strongly increased research activity can be divided into two major routes: various industrial laboratories apply chemical etching techniques which, for instance, have been shown to produce hydrogen terminated surfaces with extremely low surface recombination velocities[1–10]. Such surfaces are thought to be superior substrates for microelectronic devices[5, 10]. In addition, thin film photovoltaic cells based on crystalline silicon can be envisaged, similar to silicon nitride passivated cells[11, 12]. Besides the chemical wet processing methods, electrochemical investigations on silicon-aqueous electrolyte interfaces have been intensified considerably. The evolution of *in situ* and combined *ex situ* electrochemistry experimentation has made this interface increasingly accessible for detailed analysis[6, 13–18]. In particular, silicon surfaces exposed to fluoride containing solutions were analysed[6, 13–19] and models of silicon corrosion have been developed accordingly[20–22].

Despite the possible relevance in device application, the wet, *ie* room temperature, oxidation of silicon has been less intensively pursued. Although various reports on micromachining[23], etch stop procedures[24] and designing of surface structures[25] exist, very little is known about the microscopic properties of anodic oxides on silicon. In particular, the question how these oxides compare with thermally formed oxides with respect to microstructure, morphology, formation- and etch rate have not yet been addressed. In this article, these topics will be dealt with and since oxide formation and etching are processes occurring at a time-dependent progressing interface, the fundamental competing interfacial reactions will also be analysed.

Following mechanistic considerations on oxide formation in dry and wet environment (Section 2), a comparison of the physico-chemical properties of anodic and thermal oxides will be attempted (Section 3). The comparison is based partly on what is known from the literature on thermal oxides and on an extended *in situ* ellipsometric investigation of anodic and thermal oxidation. Since electrochemical and electroless etching are important features in such a comparison, the resulting interfaces during etching and at the end of electrochemical etching will be examined in detail in Section 4. First investigations on the dynamic behavior of oxide formation will be presented in Section 5, including microscopic investigations on light induced current oscillations.

The investigations rely on the availability of experimental techniques which are directly aimed at the respective topic. The already mentioned experimental evolution provides us with a large variety of methods some of which are applied for the investigations in this article. Among these techniques, *in situ* ellipsometry[26, 27], intensity modulated photocurrent spectroscopy (IMPS)[28], chronoamperometry, a combined electrochemistry/ultrahigh vacuum surface analysis system (CESA)[29] and simultaneous photocurrent/excess microwave reflectivity measurements[30] have been employed in the present study. As the detailed description of each technique does not appear appropriate in this context, the reader is referred to the respective references in the text.

## 2. MECHANISMS OF SILICON OXIDE FORMATION

### 2.1. Thermal oxidation

While an extensive literature exists on silicon oxidation and its modeling[31–33], the focus herein is on

the prediction of thickness vs. time dependencies, the nature of the formed oxide and on the microscopic mechanism of formation. This sub-section is meant to reveal the status of what is known in the much better investigated dry oxidation field in order to suggest what would be necessary for the development of an adequate description of wet oxidation processes.

**Oxidation and migration.** A rough schematic of the thermal oxidation in an intermediate state is shown in Fig. 1. The oxidation is carried out at elevated temperatures and the growth behavior can be depicted from Fig. 2. In a stream of dry oxygen, an amorphous  $\text{SiO}_2$  film forms on the Si crystal surface, pre-cleaned by the established RCA procedure[34]. Inspection of the temporal evolution of the data in Fig. 2 shows that a linear and a parabolic branch of the oxidation behavior  $d(t)$  can be distinguished. The process was initially described using the so-called linear-parabolic (L-P) model[35]. In this simple model, only two fluxes are considered: the flux of oxidant across the growing silicon oxide layer and the flux related to the number of  $\text{SiO}_2$  molecules formed at the Si-SiO<sub>2</sub> interface. The application of Fick's first law and integration of the resulting rate equation yields the expression

$$t - t_0 = k_p^{-1}(d^2 - d_0^2) + k_l^{-1}(d - d_0), \quad (1)$$

where  $k_p$  and  $k_l$  denote the parabolic and linear rate constants, respectively. For  $t_0 = 0$ ,  $d_0$  is the initial oxide thickness. Therefore, effects of pretreatment, initial oxides or other previous processing can be excluded from the model considerations. In particular, the initial interfacial oxide regime, extending several nm into the oxide film cannot be accounted for easily by the L-P model. One indication is provided by the analysis of Arrhenius plots for the oxidation rate constants. The Arrhenius plots based on the temperature dependence of the linear and parabolic rate constants do not give the expected straight lines but show some curvature[36]. As a consequence, the validity and limitations of the L-P-model have to be defined. This topic will be treated in Sub-section 2.3.

The identification of the migrating species is of decisive importance for the understanding and physically meaningful modeling of the oxidation process. It appears from  $^{18}\text{O}$  isotope investigations[37], combined isotope-nuclear resonance studies[38] and other experiments described in the literature[39] that the migrating species is molecular oxygen which does not interact with  $\text{SiO}_2$  unless H is present[40].

High resolution TEM measurements uncovered inhomogeneities in  $\text{SiO}_2$  films grown with dry  $\text{O}_2$ [41]. These inhomogeneities were interpreted as micropores

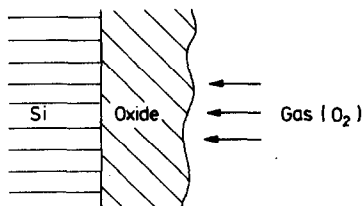


Fig. 1. Schematic drawing of the thermal oxidation of silicon.

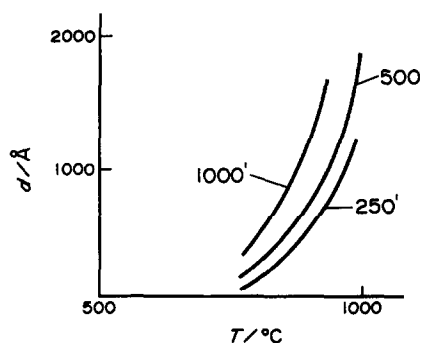


Fig. 2. Thickness vs. processing temperature of thermally formed silicon oxide; parameter, oxidation time in minutes; data evaluated from Ref. [33].

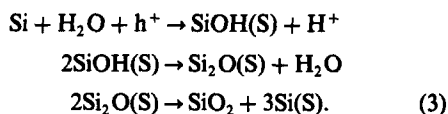
with a size of about  $10 \text{ \AA}$  in diameter. Such pores would explain the observed linear kinetic dependence by providing direct access of  $\text{O}_2$  to the transforming interface. In the etching experiments presented in Section 3, which were also performed on thermal oxides, we will make use of these features for interpretation of the results.

## 2.2. Electrochemical oxide formation

The existing data on anodization are overwhelmingly related to the study of passive films on corroding metals. Despite the amount and importance of this research, very limited direct physical information on the film properties is available to date. On semiconductors, even fewer data exist and since very recently[15, 42] only comparably indirect standard electrochemical experiments have been performed which need complementation by *ex situ* or *in situ* physical analysis methods. On silicon, an almost complete lack of information exists on the formation and physical properties of its anodic oxides. This involves the question of intermediates in the overall oxidation reaction



in which four positive charges, denoted by  $\text{h}^+$ , are consumed. The consecutive steps in the oxidation can be envisaged by the initial formation of hydroxide from water if a hole is supplied. Subsequently, two  $\text{Si}-\text{OH}$  groups form a  $\text{Si}-\text{O}$  bond splitting off a water molecule. The resulting polarization of the  $\text{Si}-\text{Si}$  backbonds then possibly leads to the insertion of O by place exchange as observed in the oxidation of platinum metal group oxygen catalysts[43, 44]:



Practically, the oxidation can be light-induced on n-type Si or potential controlled on p-Si. A schematic of these two possibilities is shown in Fig. 3. For n-Si, at a bias positive from the flat band potential,  $E_{fb}$ , illumination with light of energy  $h\nu > E_g$  results in charge separation and subsequent drift of the minority carriers to the surface (Fig. 3a). The corresponding quasi Fermi level  $P_{E_F^*}(x)$  shows the minority carrier concentration profile on a logarithmic scale.

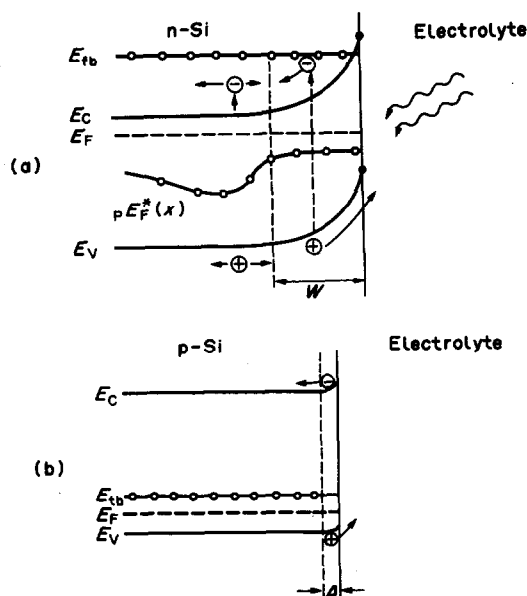


Fig. 3. Schematic drawing of the processes leading to formation of anodic oxides on silicon; (a) light induced oxide formation (n-Si); (b) potential induced oxidation (p-Si);  $W$ : depletion layer width;  $P E_F^*(x)$  quasi Fermi level of holes;  $E_c$ ,  $E_v$ ,  $E_F$ ,  $E_{fb}$ : conduction band, valence band edge, Fermi level and flat band potential, respectively.

Close to the short circuit condition at high current flow, the stationary excess carrier concentration in the depletion region of width  $W$  is comparably small as indicated in the figure. On p-Si, anodic polarization in the dark results in an accumulation layer at the semiconductor surface. This narrow layer of width of the order of several tens of angstroms is characterized by a high concentration of holes at the surface and leads to rapid oxidation. A typical cyclic voltammogram obtained for n-Si under illumination is shown in Fig. 4. Increasing passivation is seen upon repeated scans.

The short considerations on oxidation of Si in Sub-sections 2.1 and 2.2 have already demonstrated that the phase transformation of Si to  $\text{SiO}_2$  is a complicated process involving diffusion, place exchange and a transition to a different amorphous lattice geometry. At any given time, the temporary transition reveals itself at the Si-SiO<sub>2</sub> interfacial region. In the research area of thermal oxidation very intense research on this interfacial transitory oxide region has been carried out[45–52]. On anodic oxides, such data have not yet been reported.

### 2.3. Interfacial oxides

For thick thermal oxides, a division into three morphological subregions is generally made. In the initial oxidation regime which cannot be described by the L-P model, two regions are distinguished: the first part comprises the very initial oxidation of thickness of about 10 Å, the second part extends several hundred angstroms into the oxide film. Recently the study of the initial oxidation has attracted considerable interest. Usually, these experiments are performed in UHV environment on carefully cleaned (annealed) or vacuum cleaved well oriented single

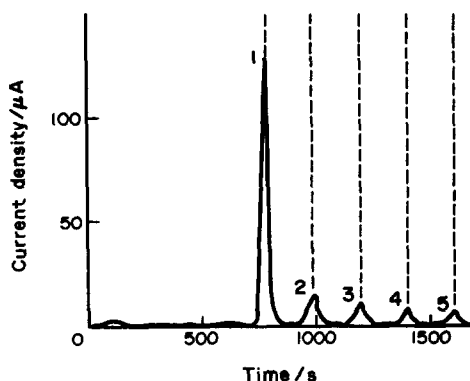


Fig. 4. Cyclic voltammogram of illuminated n-Si in phthalate buffer solution; pH = 4.5, potential referred to saturated calomel electrode (sce), 1–5: cycles between 0 and -4 V.

crystal surfaces. At present a considerable ambiguity prevails whether the Si-SiO<sub>2</sub> interface is abrupt or not. Whereas Ourzmad *et al.*[53] and Fuoss *et al.*[54] postulate a crystalline interphase which is identified as either tridymite or α-cristobalite, Himpsel *et al.* claim to observe a non-abrupt interface in which protrusions of Si<sup>3+</sup> into the SiO<sub>2</sub> layer occur[52]. These discrepancies demonstrate the importance of the details in surface preparation and oxidation procedure which obviously strongly influence the initial oxidation process. They also show that the intricacies of altered starting conditions can very well influence the SiO<sub>2</sub> morphology up to several hundred angstroms thickness[55, 56].

For the second oxidation regime various *in situ* ellipsometric investigations exist which show that also this region can be described by an L-P-law, but different L-P rate constants compared to thicker oxides have to be assumed. More recently a correlation between available bonds at the silicon surface with the linear rate constant for the oxidation rate dependence on crystal orientation has been made[57]. To describe the crossover for increased thickness in  $d(t)$  plots from (110) to (111) orientation stress models have been postulated[58]. The crossover is observed by Lewis and Irene[59] at about 5 Å thickness. Presently, further information is collected from low pressure oxidation experiments as it appears that the oxygen pressure and moisture strongly influences the properties and mechanism of the growing oxide[60].

## 3. COMPARISON OF ANODIC AND THERMAL OXIDES

In this section, combined chronoamperometric and *in situ* ellipsometry experiments on anodic oxidation of n- and p-type Si are presented. Comparison of anodic oxides with already thermally oxidized samples is done during etching of both systems in aqueous solution of NH<sub>4</sub>F. Details on the experimental procedure are given in Refs [61, 62].

### 3.1. Passivation of silicon

The optical changes induced by stepwise passivation of Si in a phthalate buffer solution are displayed

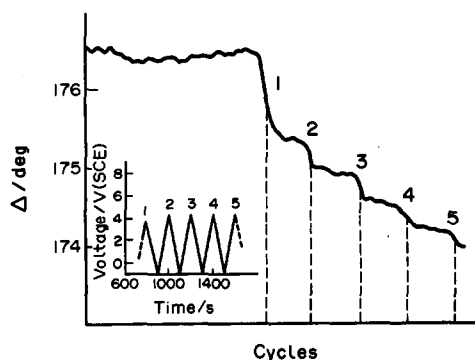


Fig. 5. *In situ* ellipsometric measurement of cyclic passivation of n-Si (111) in phthalate buffer solution; pH = 4.5, light intensity  $I = 100 \text{ mWcm}^{-2}$ ; the insert shows the voltage-time dependence.

in Fig. 5. Here, the change of the ellipsometric angle  $\Delta$  with successively increased anodic potential is shown. For transparent films  $\Delta$  can be viewed as a measure of thickness as it defines the phase in the ellipsometric function

$$\rho = \tan \Psi \exp(i\Delta), \quad (4)$$

where  $\rho$  denotes the complex ratio of the polarization dependent reflectivities  $R_p$  and  $R_s$ . The decrease in  $\Delta$  is showing the growth of a film. Figure 5 also shows that the change in  $\Delta$  becomes smaller if a layer already exists on the surface thereby indicating the decrease of the growth rate for equal increments in the applied voltage. The optical tracking of the galvanostatic oxidation of p-Si (111) is presented in Fig. 6 showing the typical eggshape behavior of  $\Delta$  vs.  $\Psi$ [62]. As can be seen from the comparison of the measured values (full circles) with the solid line obtained from a fit assuming an 800 Å thick transparent film of refractive index  $n = 1.446$ , good agreement can be achieved with relatively simple assumptions. For the initial oxidation regime, however, the fit is not as good as it might appear in Fig. 6. Closer inspection shows that the assumption of a constant

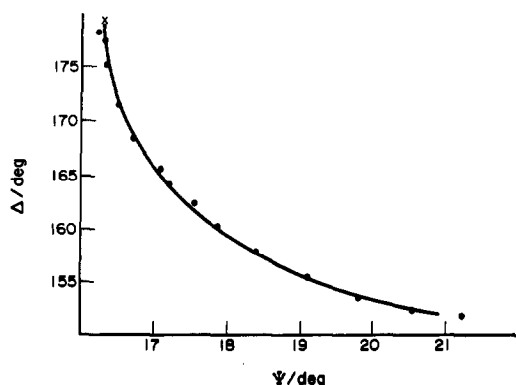


Fig. 6. Change of the ellipsometric angles  $\Delta$  and  $\Psi$  during formation of an anodic oxide on p-Si (111); oxide formation was done in the galvanostatic mode with  $i = 200 \text{ mAcm}^{-2}$  in phthalate buffer solution at pH 4.5; the solid line has been calculated assuming an 800 Å thick film with refractive index  $n = 1.446$ .

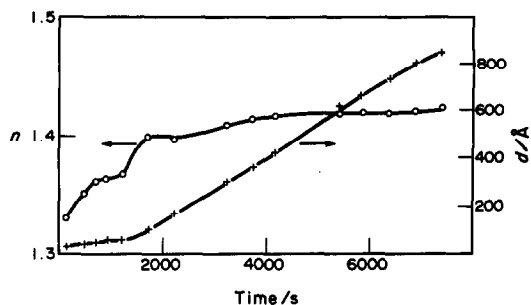


Fig. 7. Plot of refractive index  $n$  and thickness  $d$  vs. time obtained during galvanostatic oxidation of p-Si (111); compare Fig. 6.

refractive index cannot be maintained in this region. In Fig. 7, a plot of the thickness  $d$  and of the refractive index  $n$  with anodization time as calculated from the optical angles is given. The current density reached its final value at  $t = 1500 \text{ s}$ , therefore the sluggish increase in thickness in the range  $t < 1500 \text{ s}$  is due to lower applied current densities. The thickness increase for  $t > 1500 \text{ s}$  is linear and the refractive index, which is always an integral value determined from the complete oxide film, remains relatively constant at a value of  $n = 1.42$ . For a thickness of up to 500 Å ( $t \approx 1800 \text{ s}$ ), drastic changes in the refractive index are noted. Since the refractive index of water is  $n = 1.33$ , the low values for  $n$  at small  $d$  are indicative of the existence of a strongly water and/or hydroxyl groups containing layer. In addition, the comparison of the amount of charge transferred during the experiment and the thickness calculated based on charge considerations does not coincide with the optically determined thickness. Actually, only about 10% of the charge passed is converted to form the silicon oxide layer, assuming that four charges are transferred to form  $\text{SiO}_2$  out of Si. The major part of the current is likely to result in oxygen evolution, and also thickness reduction due to dissolution of smaller silicon oxide clusters by bond rupture might occur.

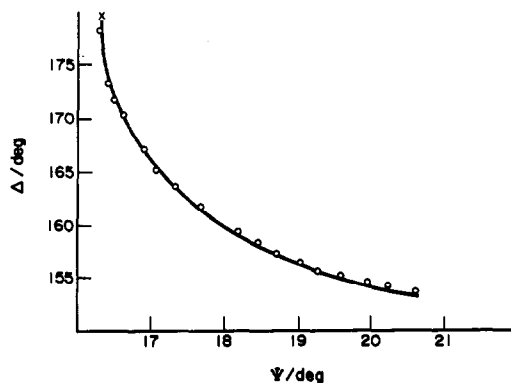


Fig. 8. *In situ* ellipsometric measurement on etching behavior of a galvanostatically formed oxide on p-Si (111) in 0.1 M  $\text{NH}_4\text{F}$ ; the solid line represents a data fit assuming  $n = 1.44$ .

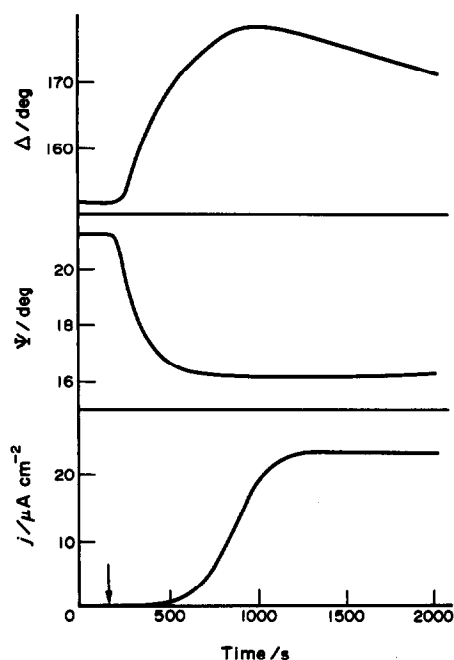


Fig. 9. Simultaneous measurement of  $\Delta$ ,  $\Psi$  and electrode current during etchback of a galvanostatically formed oxide on p-Si (111) after addition of 0.1 M  $\text{NH}_4\text{F}$ .

### 3.2. Thermal and anodic oxide dissolution

A comparison of anodic and thermal oxides can be made by ellipsometric profiling of the dissolution processes in both systems. Conveniently, an aqueous solution of  $\text{NH}_4\text{F}$  is used and Fig. 8 shows a  $\Delta$ - $\Psi$

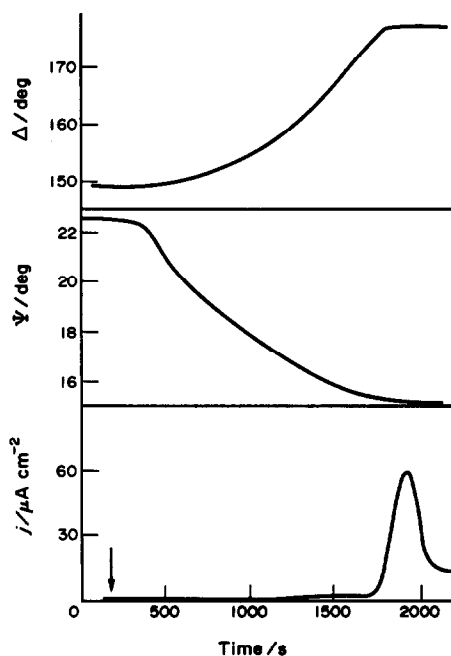


Fig. 10. Simultaneous measurement of  $\Delta$ ,  $\Psi$  and electrode current during etchback of an approximately 1000 Å thick anodic oxide on n-Si (111), formed under illumination; the arrow marks the time of addition of 0.1 M  $\text{NH}_4\text{F}$  to the buffer solution.

representation of the dissolution of a galvanic oxide. Similar to Fig. 6, good agreement with calculated data assuming  $n = 1.44$  is obtained. A more detailed view is given in Fig. 9 where the addition of  $\text{NH}_4\text{F}$  is marked by the arrow. A drastic change in  $\Delta$  and  $\Psi$  is observed.  $\Delta$  shows a maximum at about  $t = 1000$  s followed by a slow decay which is either due to film formation or roughness. This issue has not yet been clarified. Simultaneous to the initial changes in  $\Delta$  and  $\Psi$ , the rise of a current is observed at  $t \approx 500$  s. The current leveling at  $t \approx 1200$  s coincides with the maximum in  $\Delta$  whereas  $\Psi$  has reached a stationary value shortly after the current onset.

A data set from a similar dissolution experiment is shown in Fig. 10. Here anodization has been achieved by illumination of the n-Si (111) electrode and by a stepwise increase of the potential. The changes in  $\Delta$  and  $\Psi$  induced by etching in  $\text{NH}_4\text{F}$  are substantially different from those on anodized p-Si and indicate a considerably reduced average etch rate. At  $t \approx 1700$  s a steep current rise is observed and simultaneously  $\Delta$  and  $\Psi$  reach the stable values of an almost bare silicon surface. The observed current decays for increasing time. Its specific features will be treated in Section 4.

The temporal evolution of the etching behavior of a 1500 Å thick thermal oxide on n-Si (100) is given in Fig. 11. Since the etch rates of thermal oxides are substantially lower than those of anodic oxides, a 1 M  $\text{NH}_4\text{F}$  solution has been used in this case. The time dependence of  $\Delta$  and  $\Psi$  shows that the etching in 1 M  $\text{NH}_4\text{F}$  is on average still slower compared to the anodic oxides in Figs 9 and 10. At the time when the current rise is observed drastic changes appear in  $\Delta$  and  $\Psi$  which level out for  $t > 4000$  s. These changes are associated with a so-called loop in the  $\Delta$ - $\Psi$  plot

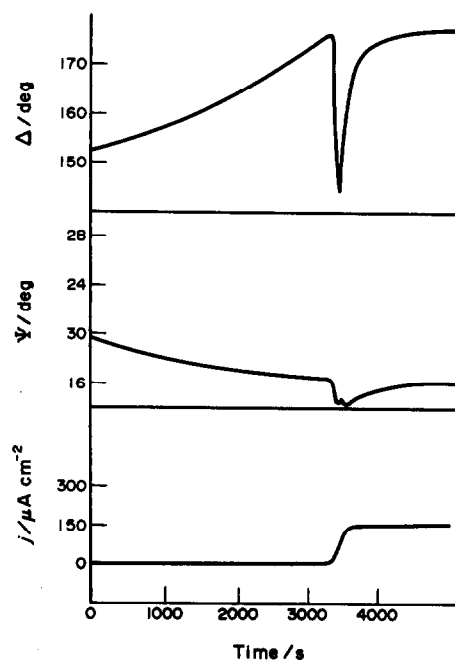


Fig. 11. *In situ* ellipsometric measurement of the etchback behavior of a 1500 Å thick thermal oxide formed on n-Si (100); solution: 1 M  $\text{NH}_4\text{F}$ , pH 5.3; potential: +0.3 V (*sce*).

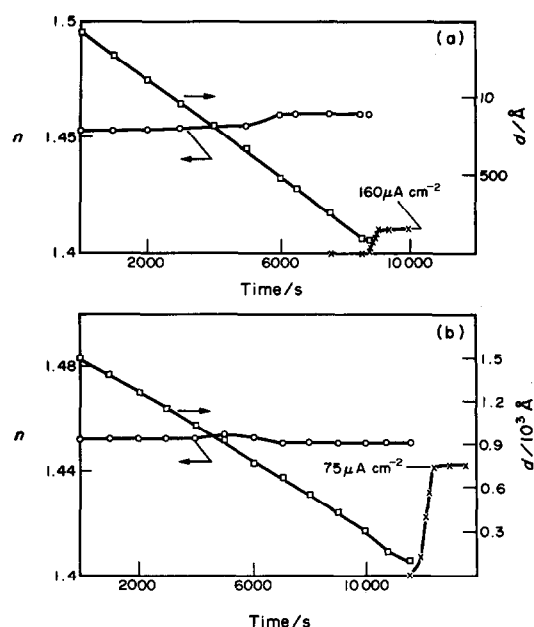


Fig. 12. Change of refractive index, thickness of oxide and current with time for etching of thermal oxides on p-Si (a) and n-Si (b) in 1 M  $\text{NH}_4\text{F}$  solution, pH 5.3; electrode potential for p-Si: +1.0 V (*sce*), n-Si: +0.3 V (*sce*).

and have been attributed to competitive oxidation and dissolution processes once the etch front has reached defective silicon oxide and the bare substrate. Due to illumination of the n-type sample the etched surface can now form an electrochemical oxide which in turn is dissolved in the fluoride containing solution and a transitory roughness is observed, as evidenced by the changes in  $\Delta$  and  $\Psi$  at  $t \approx 3300$  s[63].

The dissolution behavior of thermal oxides grown on n- and p-type Si is compared in Fig. 12. The  $t = 0$  value in Fig. 11 corresponds to  $t = 4400$  s in Fig. 12a. It can be seen that the oxide on p-Si etches faster (Fig. 12a) compared to n-Si (Fig. 12b) as the thickness at which the dark current rise occurs, *ie* approximately 60  $\text{\AA}$ , is reached at about 9000 s in the former and at 12,000 s in the latter case, indicating differences in the micropore structure mentioned in Subsection 2.1. The averaged etch rates for anodic and thermal oxides are summarized in Table 1.

It should be kept in mind that the morphology and microstructure of anodic oxides is strongly dependent on the preparation conditions and that the values given in Table 1 should only be taken as a rough measure of etch rates. The results for thermal oxidation, however, are believed to be considerably less influenced by preparation conditions as thick oxides

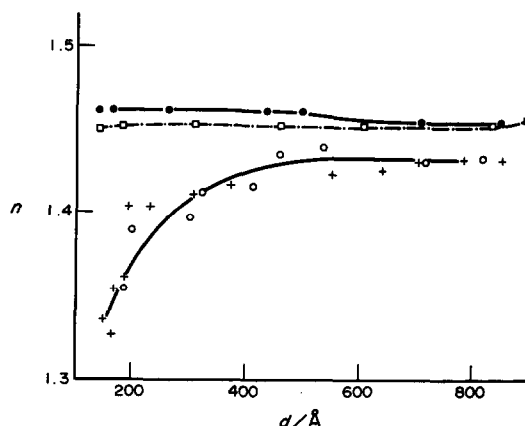


Fig. 13. Comparison of etching profiles obtained for thermal and anodic oxides on n- and p-types Si by plotting the calculated refractive index vs. oxide thickness; full circles: p-Si, thermal oxide; open rectangles: n-Si, thermal oxide; open circles: electrochemical oxide on n-Si; crosses: electrochemical oxides on p-Si.

with  $d = 1500$   $\text{\AA}$  can be prepared quite reproducibly. It has been observed, however, that the solution pH drastically influences the etching rates as will be shown below. Nevertheless the comparison of the etch rates for n-Si with thermal and anodic oxides shows differences by a factor of approximately 200.

In Fig. 13 the data on anodic and thermal oxides on p- and n-type Si are summarized in a refractive index vs. thickness plot. The general feature also observed in Fig. 7 is the reduced optical thickness of anodic oxides which clearly contain a substantial amount of water, voids and/or hydroxides. The relative incorporation of hydrous silicates obviously decreases with increasing thickness of the oxidic film and at about  $d = 500$   $\text{\AA}$  similar optical properties as for thermal oxides are observed. The lower final value for  $n$  of the anodic films results from the integrating method also summing up the initial low refractive index parts of the films.

#### 4. INTERFACIAL PROCESSES

The results in Section 3 show that a major difference between thermal and anodic oxides is found in the region near the interface, extending up to several hundred angstroms into the oxide. An additional hitherto unknown feature is the occurrence of a current at low thickness upon etching in  $\text{NH}_4\text{F}$  which should be electroless according to the overall reaction

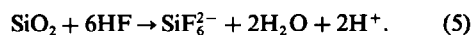


Table 1. Average etch rates for anodic and thermal oxides

Oxide type	Semiconductor	Etch rate/ $\text{\AA s}^{-1}$	Etching solution
Electrochemical oxides	n-Si (111)	0.5	0.1 M $\text{NH}_4\text{F}$ pH 4.5
	p-Si (111)	0.8	
Thermal oxides	n-Si (100)	0.003	1 M $\text{NH}_4\text{F}$ pH 5.3
		0.12	
	p-Si (100)	0.16	

As the light intensity of the ellipsometer probe beam was quite high it is not yet clear whether the currents observed in Figs 9–11 are mainly light induced. The need for fast noise-reduced recording did not allow us to reduce the light intensity in those fast automatic null ellipsometer measurements. The distinction becomes possible by applying a new coupled Faraday-modulator/rotating analyser configuration[64] which allows the measurement of  $\Delta$  and  $\Psi$  at probe light levels which do not markedly alter the observed current. Such an experiment is depicted in Fig. 14 where the dissolution of a thin (73 Å) thermal oxide (P. Lange supplied samples) is profiled. The occurring current is shown together with the superimposed light induced effect on these n-type samples. The result shows that this current is basically a dark current, which was observed first by Matsumura and Morrison[20].

#### 4.1. Dissolution processes at the Si/SiO<sub>2</sub> interface

Besides the fundamental scientific interest in what information on oxides can be obtained from analysis of dissolution experiments at the silicon–silicon oxide interface, large interest in the possibility of hydrogen termination of silicon surfaces exists. Hydrogen terminated surfaces are strongly hydrophobic, chemically very stable and exhibit superior electronic properties. Accordingly several successful reports exist which show that hydrogen passivation can be achieved by electroless HF dips. So far, however, it is not clear whether the coverage is complete and

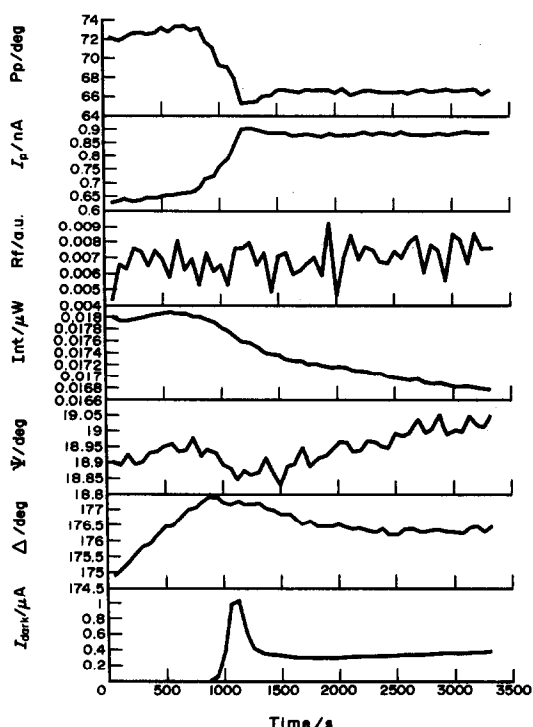


Fig. 14. *In situ* ellipsometric measurement using a modified rotating analyser configuration with a Faraday modulator for low probe light levels;  $\Delta$ ,  $\Psi$ , and dark current as well as probe light photocurrents are displayed;  $P_p$ : phase of photocurrent;  $I_p$ : photocurrent;  $R_f$ : roughness factor[27];  $\text{Int}$ : detector intensity;  $I_{\text{dark}}$ : dark current.

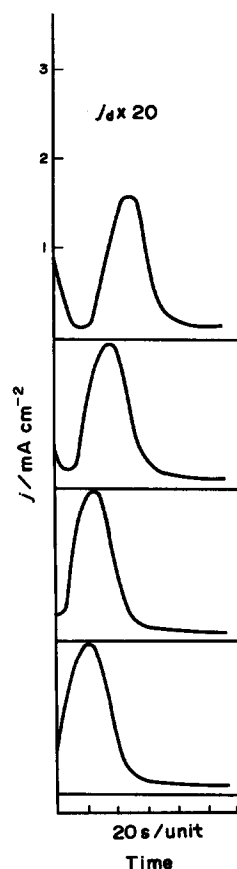


Fig. 15. Dark current transients obtained after passivation of n-Si (111) by illumination for four electrode potentials; solution: 1 M  $\text{NH}_4\text{F}$ , pH 4.5; potentials: 4, 3, 1.5 and 1 V (from top to bottom).

which species exist on the surface[1, 10]. In addition, the feasibility of hydrogen termination does depend on the crystal orientation. Therefore, the question arises whether electrochemical processing could produce similar or superior results with respect to hydrogen saturated silicon surfaces. Inspection of Figs 9–11 and 14 shows that the dark current levelling and/or decay is associated with the  $\Delta$ – $\Psi$  values of the bare, smooth silicon surface. Since the mechanism suggested for the origin of this current postulates electron injection from defect boundaries into the conduction band of Si[20], the decay of the current might be correlated with a surface exhibiting a reduced number of defect sites. Dark current transients obtained by anodization of n-Si at four potentials and after exposure to 0.1 M  $\text{NH}_4\text{F}$  solution are shown in Fig. 15. Obviously the dark current occurs at the final steps of oxide dissolution. Since the existence of pores and micropores in thermal as well as in electrochemical oxides is widely accepted and evidenced by numerous experimental observations[63, 65, 66], a model description based on changes in pore diameter during etching appears appropriate. The model uses the fact that the pore boundaries are defect sites at which, according to the dark current model, place exchange between O and F and subsequently H can occur resulting in electron injection. Then the current associated with the growth of pores is given by the

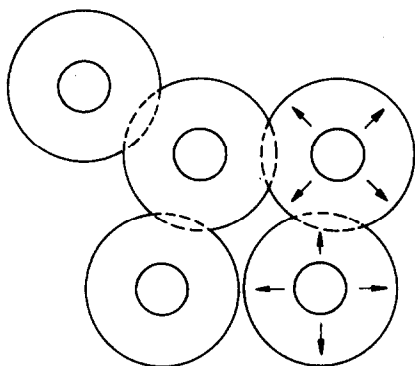


Fig. 16. Schematic representation of the functional correlation of the circumferences of overlapping circles with the sum of circumferences as given by Avrami's theorem.

cylindrical area of the pores and the problem is mathematically identical to two dimensional electrocrystallization[67]. Using Avrami's theorem concerning the overlap of the growing pores (Fig. 16) which relates the complete area (dashed plus full lines) with the resulting non-overlapping surfaces (full lines), the currents for instantaneous and progressive growth can be obtained[68] from

$$i_D = AK^2 \exp(-ct^2) \quad (6)$$

$$i_D = BK^2 t \exp(-c't^3), \quad (7)$$

where equation (6) gives the result for instantaneous growth and equation (7) for progressive growth, *i.e.* the number of pores increases linearly with time. *K* is the rate of dissolution of oxidic centers, the constants include material properties and electrochemical factors. A plot of  $i_D/i_{D_{\max}}$  vs.  $t/t_{\max}$  is given in Fig. 17 for anodization at lower and higher potential. The data points can be modeled quite well by the assumption of 2-D pore growth as can be seen by comparing them with the mathematically obtained full lines. The data indicate that thicker oxides, grown at higher anodic potential, etch according to the progressive model in which the number of pores increases with time. The deviation at  $t > t_m$  indicates that the model loses validity on a more open, bare surface, just as the electrocrystallization is not easily described in its initial steps by the model.

#### 4.2. Photocurrent multiplication

The enhancement of the nominal quantum yield beyond unity has been observed for several illumina-

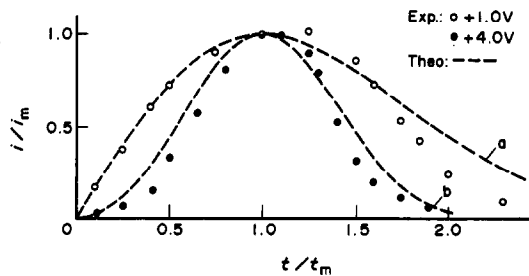


Fig. 17. Comparisons of normalized experimental and calculated (lines) dark current transients; circles:  $U = +1.0$  V (*sce*), squares:  $U = +4.0$  V (*sce*);  $i_m$  and  $t_m$  denote the dark current maximum and the time at  $i_m$ .

nated semiconductor-electrolyte systems[19, 20, 69, 70]. The effect can be attributed to the concordant injection of charge carriers from surface complexes, formed under illumination by minority carriers, into the majority carrier band. On n-type silicon for instance, the oxidation reaction involves four steps thus allowing for a maximum quantum yield multiplication factor  $m_Q$ ,

$$m_Q = \frac{n_c}{n_m} = 4, \quad (8)$$

where  $n_c$  denotes the number of charges transferred and  $n_m$  the number of light induced minority carriers in the reaction. It becomes immediately clear that the temporal behavior of minority vs. majority carrier transfer determines the value of  $m_Q$ : if the time between the collection of the first and the second hole at the silicon surface is large enough to allow the injection of one or more electrons into the conduction band  $m_Q > 1$ . This competition can be influenced by the light level (number of generated holes), the potential (drift velocity and space charge layer width), the wavelength (absorption profile), the HF concentration (etch rate) and the pH which also influences the etch rate. In addition, the energetic position and width of the charge injecting complex with respect to the band edges determines largely the injection rate. Very little is known about the microscopic nature of the injecting species, its possible energetic distribution related with a possible variety of adsorption sites and eventual partial solvation of the complex and its change in energy upon charge storage and release.

A method to at least partially disentangle such competitive processes is provided by intensity modulated photocurrent spectroscopy (IMPS)[69, 71]. Details are given elsewhere[19, 69]. In such frequency dependent experiments the quantum yield is measured as

$$Q = \frac{j_{ph}}{j_m} = \text{Re}(Q) + i \text{Im}(Q), \quad (9)$$

where  $j_{ph}$  is the nominally measured current under illumination and  $j_m$  denotes the current induced by the minority carrier reaction. Figure 18 shows an experimental result in which  $\text{Im}(Q)$  is plotted against  $\text{Re}(Q)$  for various modulation frequencies. As can be seen, the real part of  $Q$  almost reaches the value 4. Setting up a set of linear differential equations using first order rate constants, the experimental data can be modelled yielding a set of rate constants[17, 72]. In

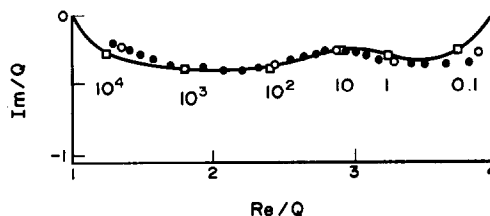


Fig. 18. Plot of imaginary vs. real part of the quantum yield in a frequency dependent intensity modulated photocurrent measurement on n-Si (111); solution: 6.5 M  $\text{NH}_4\text{F}$ , pH 5.4; electrode potential: +1.5 V (*sce*), photon flux  $< 10^{13} \text{ cm}^{-2} \text{ s}^{-1}$ ; filled circles: experiment; full line: data fit using a set of rate constants.



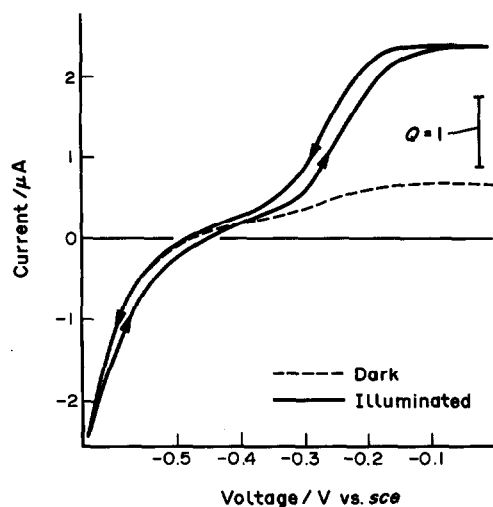


Fig. 19. Cyclic voltammogram of n-Si (111) in 1 M  $\text{NH}_4\text{F}$  at pH 5.3 in the dark (dashed line) and under illumination (full line) with monochromatic light ( $\lambda = 442 \text{ nm}$ ) of intensity  $I = 2.6 \mu\text{W cm}^{-2}$ , scan velocity  $10 \text{ mV s}^{-1}$ ; the expected value for a quantum yield equal to 1 is indicated.

the case shown in Fig. 18, the following electron injection rate constants defined by

$$\bar{j}_{\text{ph}} = j_m + \sum_{i=1}^3 k_i c_i, \quad (10)$$

where  $k_i$ ,  $c_i$  are the respective rate constants and surface concentration of the electron injection reactions are obtained:  $k_1 = 2 \times 10^4 \text{ s}^{-1}$ ,  $k_2 = 5 \times 10^2 \text{ s}^{-1}$ ,  $k_3 = 0.5 \text{ s}^{-1}$ . The latter value is indicative of a very slow reaction which might be explained by considering the chemical transformation of Si in the  $sp^3$  tetrahedral configuration (solid) to the  $sp^3d^2$  octahedral structure of the  $\text{SiF}_6^{2-}$  anion in solution.

Whereas nominal photocurrent quadrupling is experimentally quite difficult to obtain, photocurrent doubling on Si is easily achieved [15, 16, 20]. Electrodes emersed after the decay of the dark current (see Fig. 17) show photocurrent doubling upon low level illumination in ammonium fluoride solution. A typical corresponding cyclic voltammogram is shown in Fig. 19. Obviously the electrochemical treatment allowing dark current flow produces a surface with very specific properties. The elucidation of the character and the microscopic surface condition necessitate the application of *in situ* or *ex situ* surface analytical methods.

#### 4.3. Ex situ UHV-interface analysis

Besides *in situ* methods such as FTIR [6, 74], the investigation of the surface condition by electron spectroscopies provides a powerful tool in the analysis of the surface chemistry. The reliability of the results depends on the amount of contamination and the sample handling procedure. Based on the experience of surface analysis on electrochemically treated metals [74, 75], we have designed a combined electrochemistry-surface analysis system in which contamination levels could be kept extremely low. A schematic drawing of the experimental arrangement is displayed in Fig. 20 where Fig. 20b shows the

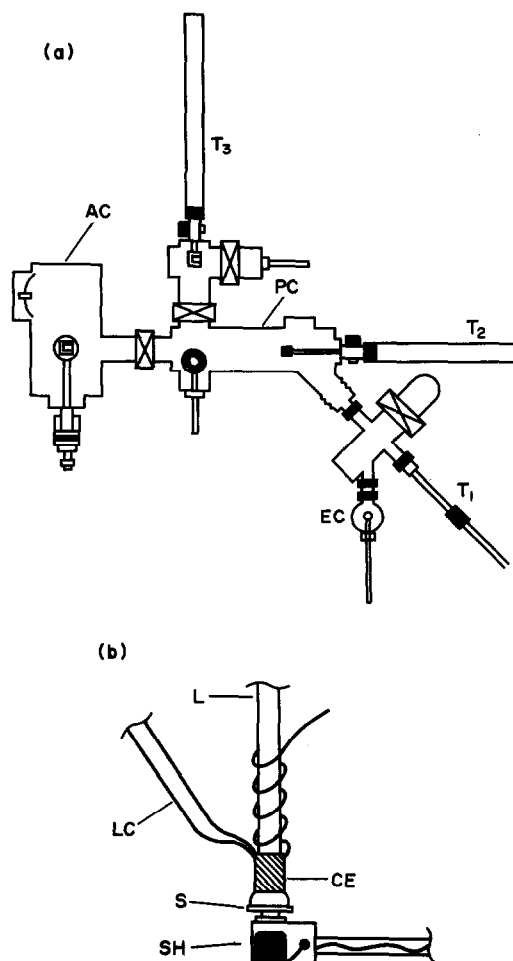


Fig. 20. Schematic drawing of the experimental arrangement for combined (photo-)electrochemistry/UHV surface analysis measurements; (a) overview of the combined system: EC, electrochemical chamber; PC, preparation chamber; T1-T3, transfer rods; AC, analysis chamber equipped for XPS, UPS, LEED; (b) detail drawing of the electrochemical chamber including sample (S) and sample holder (SH), counter- and reference electrodes (E), (RE), respectively, light guide (L) and Luggin capillary (LC).

electrochemistry vessel in more detail. The samples are kept in a slight  $\text{N}_2$  overpressure ambient during experimentation and the samples are mounted on standard UHV stubs allowing for easy transfer into the UHV preparation chamber. After degassing the sample is then transferred into the analysis chamber where X-ray photoelectron spectroscopy (XPS), ultraviolet photoelectron spectroscopy (UPS) and low energy electron diffraction (LEED) experiments could be performed.

The electrochemical conditioning curve and an XP-survey spectrum indicating a very low carbon contamination are shown in Fig. 21. From line analysis of the  $\text{C}1s$  signal, which was done for each electrochemical experiment, a hydrocarbon coverage below 0.2 monolayers (ML) could be achieved. In the following only experimental runs which exhibited such low coverages are evaluated. The samples were emersed at position a, b and c in Fig. 21 for analysis

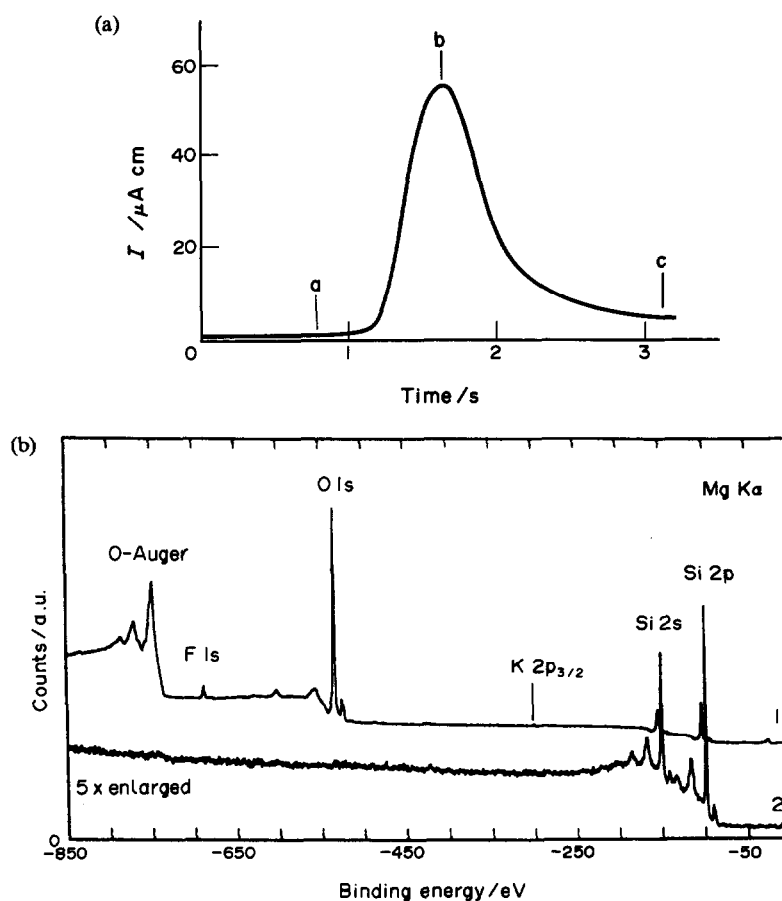


Fig. 21. XPS-survey spectrum (b) of a n-Si (111) sample emerged at position c after decay of the dark current (a) in 1 M  $\text{NH}_4\text{F}$ , pH 4.5 at  $U = 3 \text{ V}$  (*sce*).

of their surface condition. XPS line analysis data for the  $\text{Si}2p$ , the  $\text{O}1s$  and the  $\text{F}1s$  level are shown in Fig. 22. It can be seen that within the detection limit (0.1 ML) of the method, neither oxidized silicon ( $\text{SiO}_2$  line:  $E_B = 104 \text{ eV}$ ) nor any water or hydroxide

( $532 \text{ eV} \leq E_B < 534 \text{ eV}$ ) can be found on these samples. Since the absence of fluoride is also evident from Fig. 22c where a signal around  $E_B = 687 \text{ eV}$  would be expected the question arises which surface condition prevails. Figure 23 shows LEED pictures of

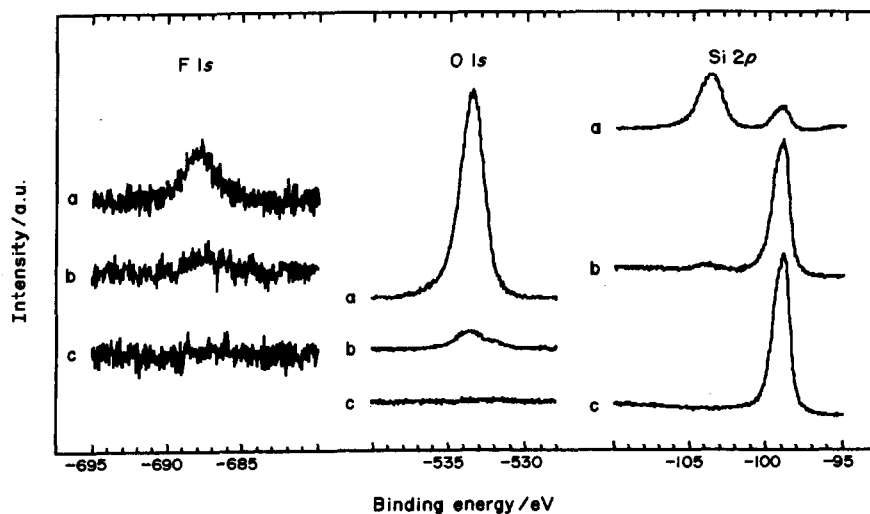


Fig. 22. XPS line analysis for a n-Si (111) sample emerged before dark current rise (a), at its maximum (b) and (c) after the dark current decay (compare Fig. 21a); the  $\text{Si}2p$ ,  $\text{O}1s$  and  $\text{F}1s$  lines are displayed.

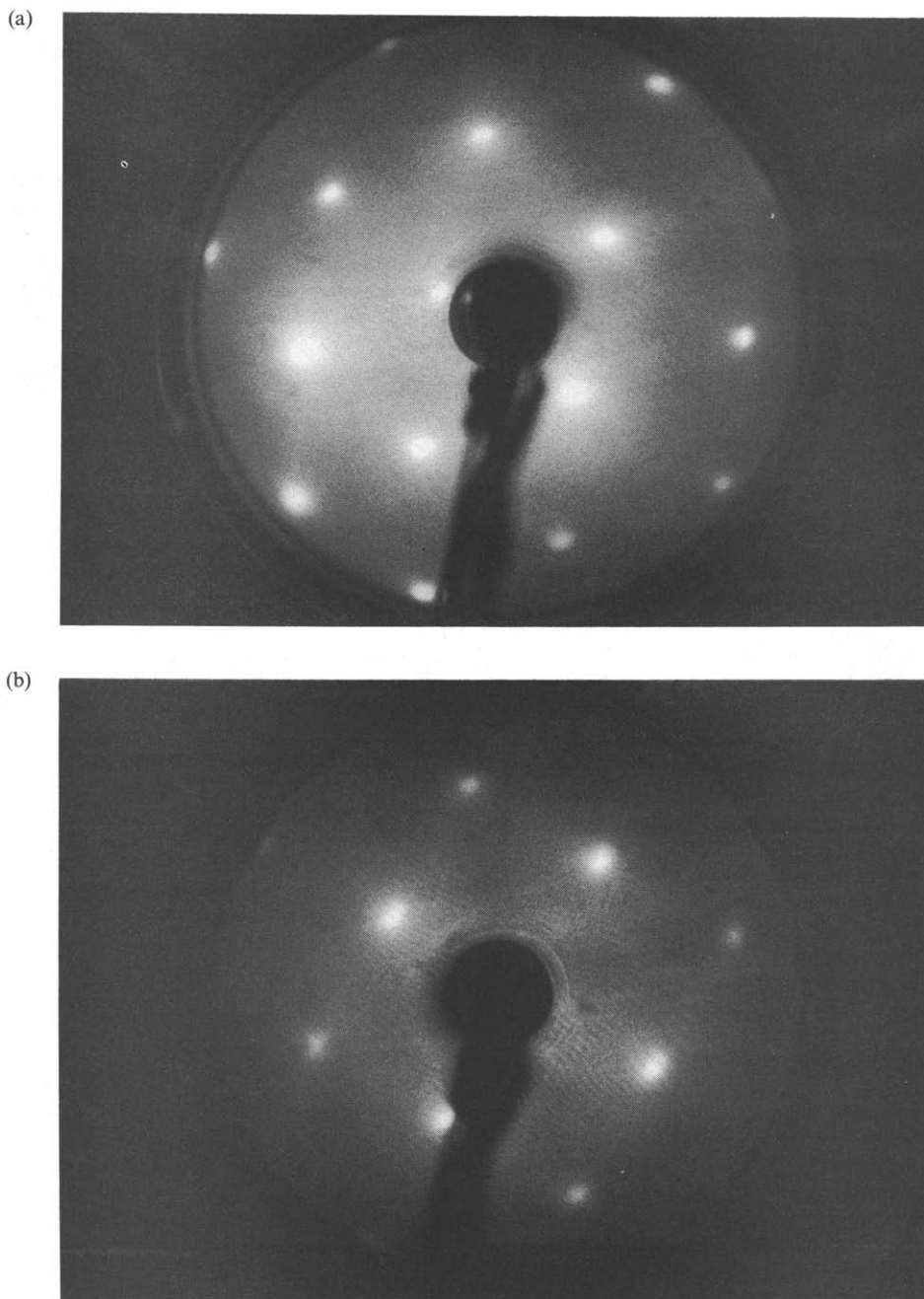


Fig. 23. Low energy electron diffraction (LEED) patterns of n-Si (111) (a) and n-Si (100) (b) samples emerged at position c in Fig. 21a; beam energy 83 eV and 65 eV, respectively.

samples emerged at position c in the curve of Fig. 21a. These first LEED data obtained on electrochemically treated semiconductors show that crystalline surfaces are prepared. The typical hexagonal threefold symmetry of the (111) surface and the cubic symmetry of the (100) surface are observed.

The first UP spectra of an electrochemically conditioned semiconductor obtained by direct sample transfer are shown in Fig. 24 for n-Si (111)[29]. Two excitation energies have been used in order to distinguish bulk from surface features. Curve 1 in Fig. 24 measured with He I excitation exhibits striking similarities with data from Himpsel *et al.*[76]

(curve 2) in the energy range between  $E_F$  and  $E_B = -6$  eV. The well known surface resonance on Si seen in angle resolved UPS as well as in photoemission yield spectroscopy around  $-0.7$  eV is quenched. Curve 2 had been obtained for a n-Si (111)—H( $1 \times 1$ ) surface and we conclude that the electrochemically prepared surface is similarly hydrogen terminated as the vacuum processed sample. For more negative binding energies, however, a new structure is observed which does not resemble those of, for instance, silicon surfaces[77]. Unfortunately, the data of Himpsel *et al.* have only been recorded down to  $E_B = -6$  eV. Comparing the He II spectrum (curve 3)

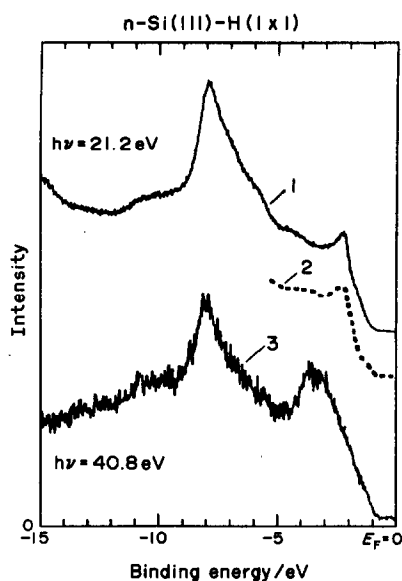


Fig. 24. UP-spectra of n-Si (111) obtained after dark current decay and subsequent emission recorded for two photon energies:  $h\nu = 21.2$  eV (He I) and  $h\nu = 40.8$  eV (He II); also shown are data measured by Himpsel *et al.* (Ref. [73]) on hydrogen-exposed vacuum cleaved Si samples.

with the He 1 spectrum (curve 1) and the literature data (curve 2) shows that the pronounced peaks at  $-7$  eV and  $-11$  eV remain unchanged in energetic position upon changing the photon energy, indicating that surface features are observed. Indeed, a very similar structure has been reported by Pandey *et al.* and was attributed to Si-SiH<sub>3</sub> complexes on the surface[77]. These results demonstrate that hydrogen terminated silicon surfaces can be prepared by a single-step electrochemical treatment exhibiting crystallinity in the sense that LEED pictures can be obtained. At present it appears more difficult to prepare similarly well hydrogen terminated Si (100) surfaces by the electrochemical treatment. The possibility of preparing hydrogen terminated surfaces[78] and of maintaining their microscopic features is obviously related to the strongly hydrophobic nature of such surfaces and their chemical inertness which makes them interesting for processing applications. The absence of fluoride on these surfaces has been discussed by Chabal and co-workers[79] who argue that the F<sup>-</sup> anion polarizes the Si-Si backbonds since electrons are inserted into the antibonding Si *d*-orbitals, resulting in bond rupture. Therefore H termination produces a more stable surface although simple binding energy considerations predict a higher stability for the Si-F bond.

## 5. DYNAMICS OF OXIDE FORMATION

The competition between oxidation and dissolution due to photo- and/or dark corrosion and etching in ammonium fluoride can be used to investigate the oxidation processes in their initial phase in more detail. If the relevant parameters are adjusted accordingly, very slow oxidation on n- and p-type samples can be studied in chronoamperometric

experiments. This initial oxidation regime was not accessible in the ellipsometric experiments (Section 3) because of an excessive probe light level.

### 5.1. Chronoamperometric oxidation

The influence of electrode potential on the passivation behavior of n-Si (111) in fluoride-containing solution is shown in Fig. 25 for constant illumination intensity. For the initial time regime, a peak with  $Q > 1$  is noted for all potentials. Whereas at  $U = 1$  V the photocurrent decays rapidly, a plateau is observed for increasing anodic potential. The plateau exists for *ca* 3 s in the case of  $U = 3$  and 4 V and subsequent passivation evidenced by a steep photocurrent decay is observed. In a similar experiment, a sample has been emerged during the plateau and transferred to UHV surface analysis measurement for investigation of the prevailing surface condition. The corresponding Si2*p* core level, the O1*s* lines and the F1*s* lines are displayed in Fig. 26. The surface consists of oxidized Si ( $E_B = 104$  eV), contains oxide ( $E_B = 533.2$  eV) as well as water and/or hydroxide ( $E_B = 532$  eV) whereas the interpretation of the high energy shoulder at  $E_B = 534$  eV is not clear. The F signal shows a maximum around  $E_B = 687$  eV which is indicative of F<sup>-</sup> and a shoulder at larger binding energy corresponding to more oxidized fluor. The presence of F-O bonds at transitory defect sites might be responsible for the hitherto unknown shoulders.

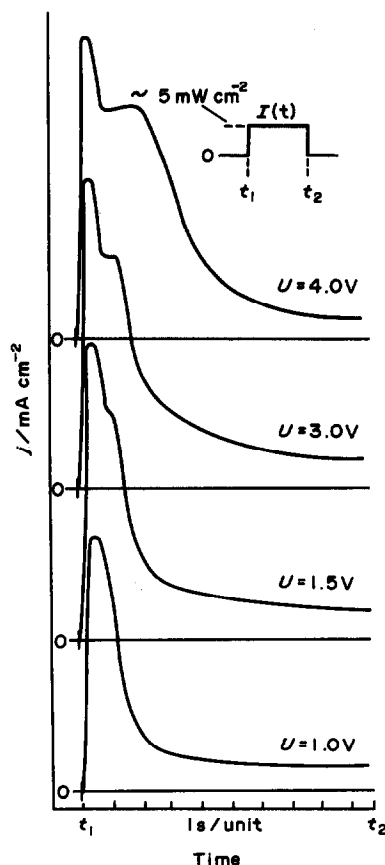


Fig. 25. Influence of electrode potential on photocurrent transients on n-Si (111) recorded in 0.1 M NH<sub>4</sub>F at pH 4.5; light intensity, 5 mW cm<sup>-2</sup>.

Table 2 gives the coverages as calculated using the closed overlayer model[80]

$$\frac{I_0}{I_{Si}} = \frac{I_0^\infty}{I_{Si}^\infty} \cdot \left[ 1 - \exp\left(\frac{d_0}{\lambda_0(E_f)\cos\theta}\right) \right] \exp\left(\frac{d_0}{\lambda_0(E_{Si})\cos\theta}\right)$$

$$\frac{I_0}{I_{Si}} \approx \frac{I_0^\infty}{I_{Si}^\infty} \left[ \frac{d_0}{\lambda_0(E_f)\cos\theta} \right] \left/ \left[ 1 - \frac{d_0}{\lambda_0(E_{Si})\cos\theta} \right] \right., \quad (11)$$

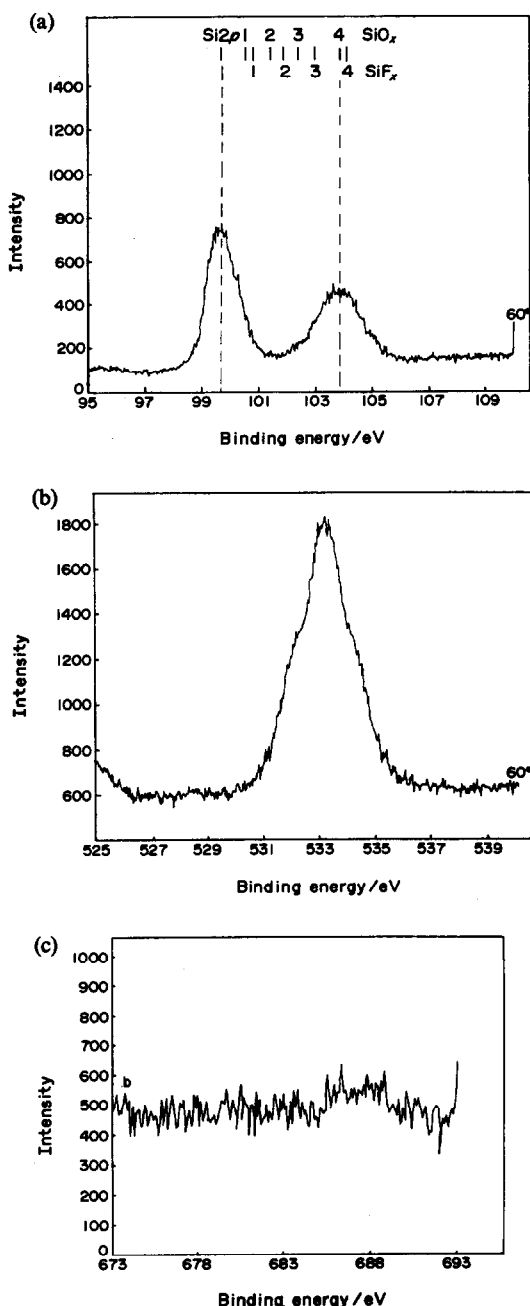
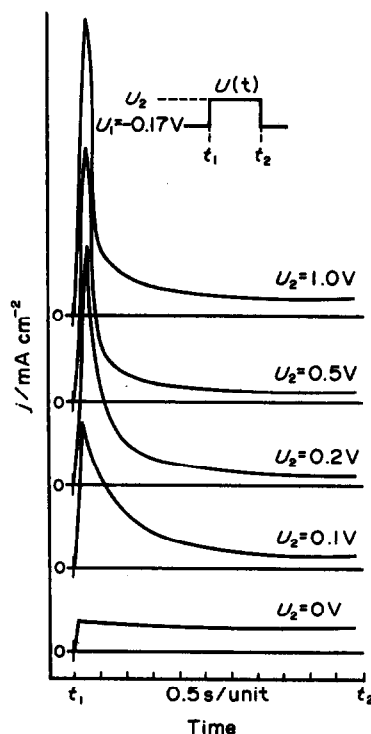
Fig. 26. XPS-line analysis of samples emerged during the plateau in the photocurrent (Fig. 26); (a) Si2p line, (b) O1s line, (c) F1s line; emission angle  $\theta = 60^\circ$ .

Table 2. Coverages calculated using closed overlayer model

Species	Coverage/ML
SiO <sub>2</sub>	2
Si-OH, H <sub>2</sub> O	0.2
SiF <sub>x</sub> , $x = 3, 4$	0.5
F-O	0.1

where  $I_0^\infty$ ,  $I_{Si}^\infty$  denote the line intensities of the pure elements,  $d_0$  the thickness of the overlayer,  $\lambda_0$  the inelastic mean free path of electrons in the Si substrate and the film and  $\theta$  is the emission angle.

Passivation on p-type Si can be readily achieved by anodic polarization as accumulation layers form. Figure 27 shows a data set for the initial time regime of the dark current. The passivation curves do not show a plateau for any potential investigated although the current densities are very similar in both cases. This finding indicates that the corrosion and passivation behavior is mediated by reaction intermediates which are energetically located within the semiconductor band gap. Obviously the electron/hole occupation of the intermediates is of crucial importance for the initial oxide growth. Otherwise, for identical currents the position of the quasi Fermi level of illuminated n-Si should coincide with the majority carrier Fermi level of p-Si at the surface[81] and no differences in oxide growth mechanism should then occur.

Fig. 27. Influence of electrode potential on dark current passivation transients of p-Si (111) in 0.1 M NH<sub>4</sub>F at pH 4.5.

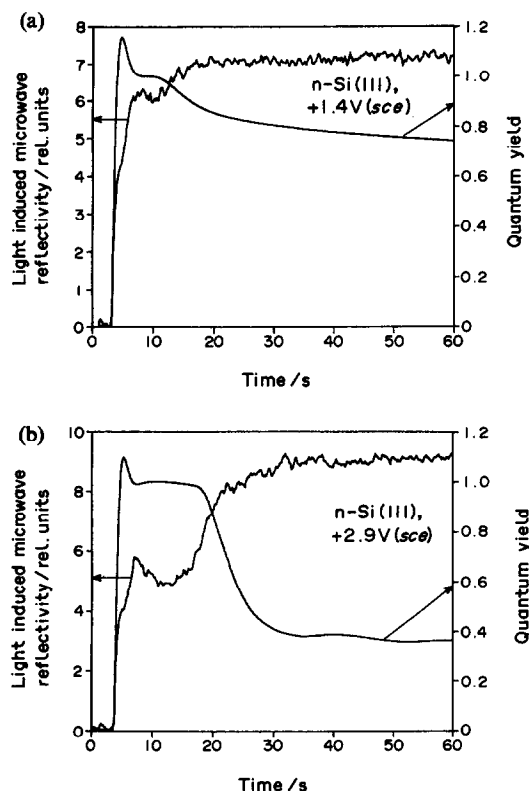


Fig. 28. Photocurrent and excess microwave reflectivity transients recorded on n-Si (111) in 0.2 M  $\text{NH}_4\text{F}$  at pH = 4.6 for (a)  $U = +1.4 \text{ V (sce)}$  and (b)  $U = 2.9 \text{ V (sce)}$ ; light intensity:  $I = 1.25 \text{ mW cm}^{-2}$ .

## 5.2. Stationary excess microwave reflectivity measurements

The information collected by *in situ* ellipsometry, chronoamperometry and *ex situ* XPS mainly concerns the morphology and chemical composition of oxides on silicon. Additional insight into the relevant electronic properties of the Si/SiO<sub>2</sub>/electrolyte system can be obtained by the simultaneous measurement of photocurrent transients and excess microwave reflectivity. The application of microwave signal analysis for semiconductor material development[82] and for the study of electrochemical processes has been attempted during recent years[84] and a detailed description is given in this issue. The experimental arrangement used in the measurements is described elsewhere[82, 84].

The experiments were performed on n-Si (111) electrodes prepared in the same way as described in Sub-section 5.1 (compare Fig. 25). Simultaneous photocurrent and excess microwave reflectivity profiles for two electrode potentials are shown in Fig. 28. The photocurrent transients resemble those of Fig. 25 with respect to their general shape but it should be kept in mind that the light intensity was lower, the fluoride concentration increased and the potentials are different. The general features, an initial quantum yield larger than unity, a decay into a plateau, where the quantum yield is close to unity and a subsequent decay with more or less pronounced passivation is

observed. The decay of  $i_{\text{ph}}$  for  $t > 20 \text{ s}$  in Fig. 28a would usually be interpreted as passivation. From photocurrent measurements alone, however, it is difficult to judge whether charge transfer is inhibited by the formed oxide layer or whether the band edge shift resulting from a potential drop across the oxide flattens the bands thus increasing the recombination rate at the Si/SiO<sub>2</sub> interface. The almost complementary behavior of the microwave signal which increases when the photocurrent decreases suggests that additional information can be obtained by the simultaneous measurement.

As an example we consider the time region of the plateau in Fig. 28b. Whereas  $i_{\text{ph}}$  remains constant, the microwave signal  $m_w$  decreases and then increases again ( $8 \text{ s} \leq t \leq 20 \text{ s}$ ). In a very simple consideration one assumes that[83]  $m_w \propto \Delta n_h(0)$  and  $i_{\text{ph}} = ek_r \Delta n_h(0)$ ;  $\Delta n_h(0)$  denotes the light induced excess minority carrier concentration at the surface  $x = 0$ . The decay of the microwave signal is then interpreted as a decay of the stationary excess hole concentration at the surface. Such a decay could be caused by either an increase in the charge transfer rate  $k_r$  or in the surface recombination velocity  $S_r$ . Since the photocurrent remains constant in this region and  $Q \approx 1$  it is concluded that the charge transfer rate changes. The initial increase of  $k_r$  is possibly due to direct bonding of reaction intermediates (inner sphere charge transfer) the decrease of  $k_r$  can be attributed to the increased thickness of the growing layer which still sustains the full photocurrent.

In a more detailed analysis, the phenomenological separation of  $k_r$  and  $S_r$  become possible. The stationary microwave signal is given by[84]

$$m_w \propto \int \Delta n_h(x) dx \quad (12)$$

with

$$\Delta n_h(x) = \Delta n_h(\text{dr.}) + \Delta n_h(\text{diff.}), \quad (13)$$

where the overall signal results from the superposition of the drift and diffusion component. The terms in equation (12) and (13) can be determined

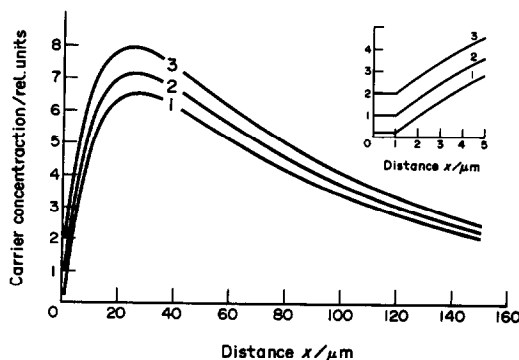


Fig. 29. Stationary excess minority carrier profiles calculated for the typical parameters of crystalline Si ( $L_p = 100 \mu\text{m}$ ,  $I_0 = 100 \text{ mW cm}^{-2}$ ,  $W = 1 \mu\text{m}$ ) for three surface concentrations of holes (n-type sample) [see equations (14, 15)].

analytically[85] by solving the appropriate transport equation[86] yielding

$$\Delta n_h(\text{dr.}) = c_1 \exp(-\alpha x) \exp[\alpha(x-w)] - 1 \quad (14)$$

$$\Delta n_h(\text{diff.}) = c_2 \exp\left(-\frac{x-w}{L_p}\right) + \gamma \exp(-\alpha w) \times \left\{ \exp\left(-\frac{x-w}{L_p}\right) - \exp[-\alpha(x-w)] \right\}, \quad (15)$$

where  $c_2$  is the non-vanishing excess carrier concentration at  $x = w$  which is assumed to be zero in Gärtner's model of efficient charge transfer[87],  $\gamma$  is a function of absorption coefficient  $\alpha$ , diffusion length  $L_p$  and light flux  $I_0$ . The surface properties are included in  $c_1$  and  $c_2$ . Minority carrier profiles for two surface minority carrier concentrations are shown in Fig. 29. In the calculation, the simplified assumption of a constant electrical field in the space charge layer has been made. It is seen that the integral [equation (12)] is at least a monotonic function of the surface carrier concentration  $\Delta n_h(0)$ . Hence

$$m_w^* = c^* \Delta n_h(0), \quad (16)$$

assuming

$$c^* = f(x, \alpha, L_p, w, I_0)$$

and

$$\Delta n_h(0) = f(c^*, k_r, S_r).$$

These considerations are made for any given time  $t$  and since the experimental changes are slow with respect to the response time of the microwave method, the processes can be viewed as quasi-stationary. The correlation of  $i_{ph}$  and  $m_w$  is possible by considering the quantum yield

$$Q = a_2 k_r \Delta n_h(0) = a_2 k_r m_w^* \quad (17)$$

and

$$Q = c \frac{i_{ph}}{I_0} \quad (18)$$

$$k_r = a_2 \frac{Q}{m_w^*}. \quad (19)$$

Assuming that carriers which recombine at the surface do not contribute to the external photocurrent, the ratio

$$\frac{k_r}{S_r} = \frac{Q}{1-Q} \quad (20)$$

can be defined. With  $S_r = k_r(1-Q)/Q$  and using equations (18) and (19) the surface recombination velocity can also be derived from the experimental data  $i_{ph}$  and  $m_w$ :

$$S_r = a_2 \frac{1-Q}{m_w^*}. \quad (21)$$

For slowly changing systems equations (19) and (21) should hold and a qualitative assignment how  $k_r$  and  $S_r$  change with measuring time becomes possible. Figure 30 shows the evaluation of the data in Fig. 28 with respect to  $k_r(t)$  and  $S_r(t)$ . As qualitatively discussed above,  $k_r$  shows a shoulder in Fig. 30 in the time regime between 8 s and 20 s. The missing data for  $S_r$  in the initial regime should not be interpreted by vanishing surface recombination. Since the scale is

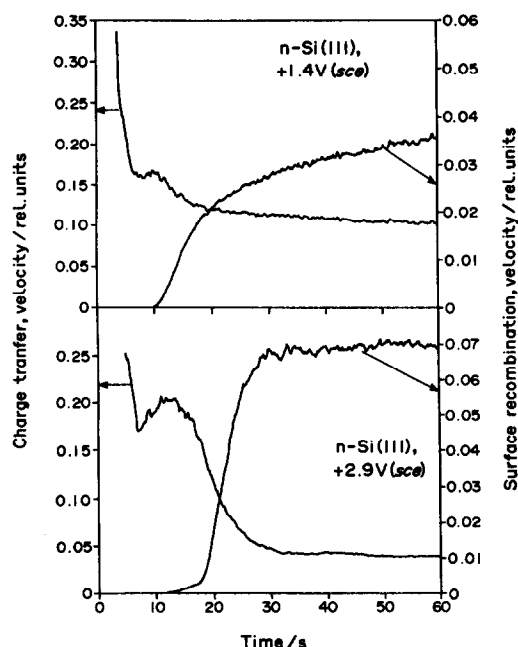


Fig. 30. Plot of the temporal evolution of  $k_r$  and  $S_r$  for the data given in Fig. 28 using equations (19) and (21).

non-logarithmic a value of  $S_r/k_r < 10^{-2}$  would be hardly visible. The determination of absolute values for  $k_r$  and  $S_r$  is therefore not possible but relative changes with time can be followed conveniently.

### 5.3. Oscillating reactions

Photo- as well as dark current oscillations have been observed on Si electrodes exposed to fluoride containing solutions[88, 89]. A satisfying microscopic explanation for the oscillation mechanism has not yet been attempted. It is clear that much more data are needed in order to be able to come up with a reasonable model. In this sub-section, new data on oscillating photocurrents as n-Si(111) in  $\text{NH}_4\text{F}$  are presented. Their analysis, however, does not yet allow development of a mechanistic model or to set up a corresponding differential equation. The preliminary results presented below are meant to show the complexity of the oxide formation and dissolution process and address some of the open questions still remaining.

Figure 31 shows sustained photocurrent oscillations at n-Si(111) measured in the electrochemical cell attached to the UHV-analysis system described in Fig. 20. For identification of the surface condition, sample emersion was done in the photocurrent minimum and maximum. Subsequent XPS surface analysis has been done and the results with respect to coverage changes are given in Table 3. The coverage determination was done using the closed overlayer model [equation (11)] which converges with the results from the fractional overlay model[81] for low (submonolayer) coverages[15]. The evaluation shows that the thickness of the oxide layer changes at most by ten percent which amounts to 1 ML in case of the 35–40 Å thick oxide present. It appears that from inspection of the  $\text{O}1s$  line at  $E_b = 532.6 \text{ eV}$ , the integrated water content of the oxides is lower at the maximum and increased at the minimum. Electron

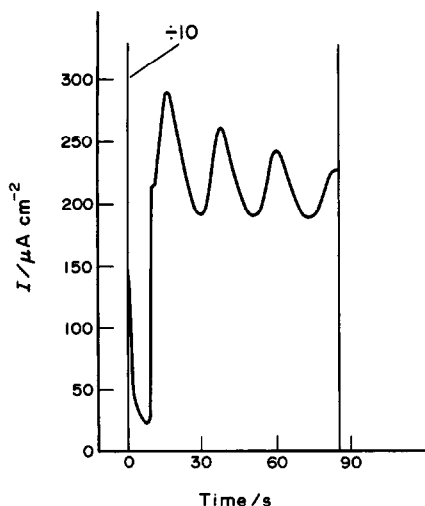


Fig. 31. Oscillating photocurrent measured on n-Si (111) in 0.1 M  $\text{NH}_4\text{F}$ , pH = 4 at  $U = +3\text{ V}$  (sce), light intensity:  $9\text{ mW cm}^{-2}$ .

emission angle measurements which allow us to enhance the surface sensitivity show that changes in the water and/or hydroxide content mostly occur at the Si-SiO<sub>2</sub> interface and possibly not at the geometrical SiO<sub>2</sub>-electrolyte boundary. Scanning tunneling microscopy shows, however, that the surfaces emersed under oscillatory conditions exhibit a considerable roughness[90]. Thus the applicability of the applied coverage model must be questioned and the emission angle measurements only give a rough estimate of the surface condition. The question still remains how very small thickness changes (10%) can be associated with strong photocurrent changes. Similar observations have been made very recently by *in situ* ellipsometry[91].

Figure 32 shows simultaneous photocurrent and excess microwave reflectivity oscillations under experimental conditions where stability breakdown has been deliberately attempted. As can be seen from Fig. 32a, instead of regular oscillations interferences and more irregular behavior are observed in both signals,  $i_{ph}$  and  $m_w$ . The separation of the signals for separate consideration of  $S_r$  and  $k_r$ , done according to equations (19) and (21), however, leads to still harmonic signals for  $S_r$  and  $k_r$  which change in magnitude with time.

Table 3. Calculated oxide thickness from XPS measurements at two emission angles

	$\theta/^\circ$	$d/\text{\AA}$
1. Current min.	90	34.5
	52	35.0
1. Current max.	90	36.5
	52	37.5
2. Current min.	90	28.5
	52	33.5
2. Current max.	90	35.0
	52	34.5
3. Current min.	90	34.5
Const. current	90	42.5
	52	43.0

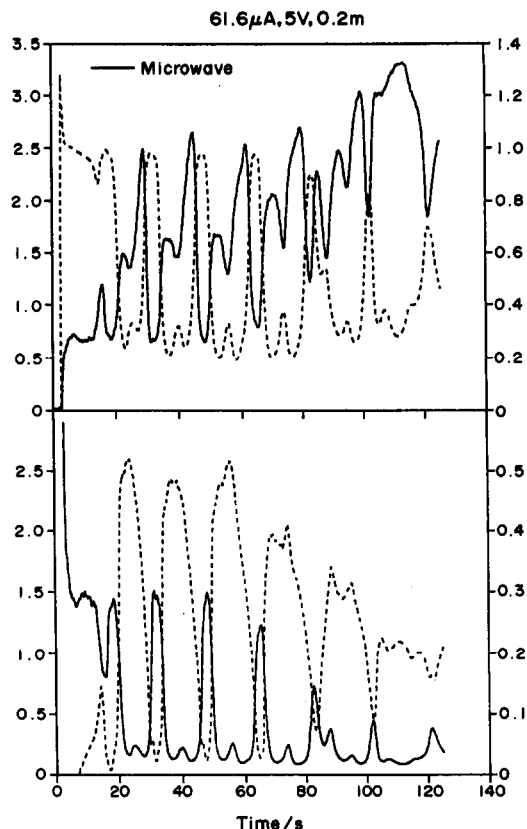


Fig. 32. Photocurrent and excess microwave reflectivity transients during oscillatory behavior (a); (b) temporal behavior of  $k_r$  and  $S_r$  determined by equations (19) and (21); solution: 0.2 M  $\text{NH}_4\text{F}$ , pH = 4.6, electrode potential:  $+2.9\text{ V}$ , light intensity:  $1.25\text{ mW cm}^{-2}$ .

## 6. SYNOPSIS

Although the combination of standard electrochemistry with modern *in situ* and *ex situ* interface analysis methods has already yielded specific and important information, the feeling is that we are merely at the basis of understanding the complex behavior of Si in aqueous electrolytes. Still very little is known about the details of the oxide growth mechanism, the influence of experimental parameters on micromorphology and general structural evolution for increased thicknesses. In some cases information can be extracted from the dissolution process (electrochemical profiling) but in particular the interface conditions are difficult to analyse. It appears that the photo- and dark electrochemistry on silicon provides a wealth of new effects, including oscillatory behavior under illumination and in the dark. Besides relevance for fundamental investigations the control of the silicon-solution interphase and the design of thin low temperature, oxide layers are of considerable interest for electronic applications and devices.

**Acknowledgements**—The author is indebted to L. M. Peter, R. Greef, J. Stumper, T. Bitzer, C. Pettenkofer, G. Schlichthörl and S. Kubala for their experimental contributions and important discussions. Additional discussions



with H. Gerischer, H. Tributsch, N. Dietz and L. Cramer are gratefully acknowledged. The work was financed in part by a BMFT grant No. 0328926A.

## REFERENCES

1. B. R. Weinberger, G. G. Peterson, T. C. Eschrich and H. A. Krasinsky, *J. appl. Phys.* **60**, 3232 (1986).
2. T. Takahagi, I. Nagai, A. Ishitani and H. Kuroda, *J. appl. Phys.* **64**, 3516 (1988).
3. E. Yablanovitch, D. L. Allara, C. C. Chang, T. Gmitter and T. B. Bright, *Phys. Rev. Lett.* **57**, 249 (1986).
4. V. A. Burrows, Y. J. Chabal, G. S. Higashi, K. Raghavachari and S. B. Christman, *Appl. Phys. Lett.* **53**, 998 (1988).
5. J. M. C. Thornton and R. H. Williams, *Phys. Scripta* **41**, 1047 (1990).
6. L. M. Peter, D. J. Blackwood and S. Pons, *Phys. Rev. Lett.* **62**, 308 (1989).
7. J. J. Boland, *Phys. Rev. Lett.* **65**, 3325 (1990).
8. G. W. Trucks, K. Raghavachari, G. S. Higashi and Y. J. Chabal, *Phys. Rev. Lett.* **65**, 504 (1990).
9. P. Dumas, Y. J. Chabal and G. S. Higashi, *Phys. Rev. Lett.* **65**, 1124 (1990).
10. D. B. Fenner, D. K. Biegelsen and R. D. Bringans, *J. appl. Phys.* **66**, 419 (1989).
11. R. Hezel and K. Jäger, *J. electrochem. Soc.* **136**, 518 (1989).
12. R. Hezel and K. Jäger, *Proc. 20th IEEE Photovolt. Spec. Conf.*, Las Vegas, p. 1560 (1988).
13. H. J. Lewerenz and J. Stumper, *Ber. Bunsenges. phys. Chem.* **92**, 1350 (1988).
14. H. J. Lewerenz, J. Stumper, C. Pettenkofer and R. Greef, *Electrochim. Acta* **34**, 1729 (1989).
15. J. Stumper, H. J. Lewerenz and C. Pettenkofer, *Phys. Rev. B* **41**, 1592 (1990).
16. J. Stumper, H. J. Lewerenz and C. Pettenkofer, *Electrochim. Acta* **34**, 1379 (1989).
17. L. M. Peter, J. Li, R. Peat, H. J. Lewerenz and J. Stumper, *Electrochim. Acta* **35**, 1657 (1990).
18. J. Stumper and H. J. Lewerenz, *J. electroanal. Chem.* **274**, 11 (1989).
19. H. J. Lewerenz, J. Stumper and L. M. Peter, *Phys. Rev. Lett.* **61**, (1989). (1988).
20. M. Matsumura and S. R. Morrison, *J. electroanal. Chem.* **147**, 157 (1983).
21. H. Gerischer and M. Lübke, *Ber. Bunsenges. phys. Chem.* **92**, 573 (1988).
22. H. Gerischer and M. Lübke, *Ber. Bunsenges. phys. Chem.* **91**, 394 (1987).
23. U. Schnakenberg, W. Benecke and B. Löchel, *Proc. 5th International Conf. Sol. State Sensors and Actuators & Eurosensors III*, Montreux, Switzerland (1989).
24. B. Kloeck, S. D. Collins, N. F. de Rooij and R. L. Smith, *IEEE Transact. Electron. Devices* **36**, 663 (1989).
25. H. Seidel, L. Csepregi, A. Heuberger and H. Baumgärtel, *J. electrochem. Soc.* **137**, 3612 (1990).
26. R. Greef and C. F. W. Norman, *J. electrochem. Soc.* **132**, 2362 (1985).
27. L. Cramer, H. Duwe, H. Jungblut, P. Lange and H. J. Lewerenz, *Surf. Sci.*, in press.
28. L. M. Peter and J. Li, *J. electroanal. Chem.* **165**, 41 (1984).
29. H. J. Lewerenz and T. Bitzer, *J. electrochem. Soc.*, in press (1992).
30. H. J. Lewerenz, G. Schlichthörl and H. Tributsch, submitted.
31. E. A. Irene, in *CRC Critical Reviews in Solid State and Materials Science*, **14**, 175 (1988).
32. B. E. Deal and A. S. Grove, *J. appl. Phys.* **36**, 3770 (1965).
33. A. Atkinson, *Rev. Mod. Phys.* **57**, 437 (1985).
34. W. Kern, *J. electrochem. Soc.* **137**, 1887 (1990).
35. A. G. Revesz and R. J. Evans, *J. Phys. Chem. Solids* **30**, 551 (1969).
36. H. Z. Massoud, J. Plummer and E. A. Irene, *J. electrochem. Soc.* **132**, 1745 (1985).
37. J. R. Ligenza and W. G. Spitzer, *J. Phys. Chem. Solids* **14**, 131 (1960).
38. E. Rosencher, A. Straboni, S. Rigo and G. Amsel, *Appl. Phys. Lett.* **34**, 254 (1979).
39. R. Pfeffer and M. Ohring, *J. appl. Phys.* **52**, 777 (1981).
40. S. Rigo, F. Rochet, B. Agius and A. Straboni, *J. electrochem. Soc.* **129**, 867 (1982).
41. E. A. Irene, *J. electrochem. Soc.* **125**, 1708 (1978).
42. M. Sander, H. J. Lewerenz and W. Jaegermann, *Ber. Bunsenges. phys. Chem.* **91**, 416 (1987).
43. H. J. Lewerenz, S. Stucki and R. Kötz, *Surf. Sci.* **126**, 463 (1983).
44. B. E. Conway, in *Electrodes of Conductive Metallic Oxides*, Part B, (Edited by S. Trasatti), p. 433. Elsevier, New York (1981).
45. B. Agius, S. Rigo, R. Rocket, M. Froment, C. Maillot, H. Roulet and G. Dufour, *Appl. Phys. Lett.* **44**, 48 (1984).
46. W. A. Tiller, *J. electrochem. Soc.* **128**, 689 (1981).
47. J. P. Hirth and W. A. Tiller, *J. appl. Phys.* **56**, 947 (1984).
48. F. J. Grunthaner and P. J. Grunthaner, in *Materials Science Reports*, **1**, 65 (1986).
49. D. Sengupta and R. N. Panigrahi, *J. Phys. D, Appl. Phys.* **14**, 503 (1981).
50. D. E. Aspnes and J. B. Theeten, *J. electrochem. Soc.* **127**, 1359 (1980).
51. E. A. Irene and E. A. Lewis, *Appl. Phys. Lett.* **51**, 767 (1987).
52. F. J. Himpsel, F. R. McFeely, A. Taleb-Ibrahimi and J. A. Yormaff, *Phys. Rev. B* **38**, 6084 (1988).
53. A. Ourzmad, D. W. Taylor, J. A. Rentschler and J. Bevk, *Phys. Rev. Lett.* **59**, 213 (1987).
54. P. H. Fuoss, L. J. Norton, S. Brennan and A. Fischer-Colbrie, *Phys. Rev. Lett.* **60**, 600 (1988).
55. P. Lange and W. Windbracke, *Thin Solid Films* **174**, (1989).
56. H. Ibach, H. D. Bruchmann and H. Wagner, *Appl. Phys. A* **29**, 113 (1982).
57. E. A. Irene, H. Z. Massoud and E. Tierney, *J. electrochem. Soc.* **133**, 1253 (1986).
58. E. P. Farnisse, *Appl. Phys. Lett.* **30**, 290 (1977).
59. E. A. Lewis and E. A. Irene, *J. electrochem. Soc.* **134**, 2332 (1987).
60. F. Rocket, S. Rigo, M. Froment, C. d'Anterrosches, C. Maillot, H. Roulet and G. Dufour, *Adv. Phys.* **35**, 237 (1986).
61. C. F. W. Norman, Ph.D. Thesis, Southampton University, U.K. (1986).
62. R. M. A. Azzam and N. M. Bashara, *Ellipsometry and Polarized Light*. North Holland, Amsterdam (1977).
63. J. Stumper, R. Greef and H. J. Lewerenz, submitted.
64. L. Cramer, H. Duwe and H. J. Lewerenz, Patent application No. DE 51/0491 DE.
65. J. M. Gibson and D. W. Dong, *J. electrochem. Soc.* **127**, 2722 (1980).
66. J. K. Srivastava and J. B. Wagner Jr., *Proc. Electrochem. Soc. Meeting*, Cincinnati (1984).
67. A. Bewick, M. Fleischmann and H. R. Thirsk, *Trans. Faraday Soc.* **58**, 2200 (1962).
68. J. A. Harrison and H. R. Thirsk, *A Guide to the Study of Electrode Kinetics*. Academic Press (1972).
69. J. Li and L. M. Peter, *J. electroanal. Chem.* **182**, 399 (1985).
70. R. Peat and L. M. Peter, *J. electroanal. Chem.* **209**, 307 (1986).

71. L. M. Peter and J. Li, *J. electroanal. Chem.* **193**, 27 (1985).
72. L. M. Peter, A. M. Borazio, H. J. Lewerenz and J. Stumper, *J. electroanal. Chem.* **290**, 229 (1990).
73. S. Bewick, K. Kunimatsu and B. S. Pons, *Electrochim Acta* **25**, 465 (1980).
74. P. N. Ross, *Surf. Sci.* **102**, 463 (1981).
75. R. Kötz, H. J. Lewerenz, P. Brüesch and S. Stucki, *J. electroanal. Chem.* **150**, 209 (1983).
76. F. J. Himpsel, P. Heimann and D. E. Eastman, *Phys. Rev.* **B24**, 2003 (1981).
77. K. C. Pandey, T. Sakurai and H. D. Hagstrum, *Phys. Rev. Lett.* **35**, 1728 (1975).
78. J. J. Boland, *Phys. Rev. Lett.* **65**, 3325 (1990).
79. G. W. Trucks, K. Raghavachari, G. S. Higashi and Y. J. Chabal, *Phys. Rev. Lett.* **65**, 504 (1990).
80. D. Briggs and M. P. Seah, *Practical Surface Analysis*, p. 211. Wiley, New York (1983).
81. R. Reinecke, Presentation at Workshop on *Wet Processing of Semiconductors*, Berlin, Germany (1989).
82. B. Messer and H. Tributsch, *J. electrochem. Soc.* **133**, 2212 (1986).
83. M. Kunst, G. Beck and H. Tributsch, *J. electrochem. Soc.* **131**, 954 (1984).
84. B. Messer and H. Tributsch, *Chem. Phys. Lett.* **142**, 546 (1987).
85. E. Kreyszig, *Advanced Engineering Mathematics*. Wiley, New York (1988).
86. S. M. Sze, *Semiconductor Devices*. Wiley, New York (1981).
87. W. W. Gärtner, *Phys. Rev.* **116**, 84 (1954).
88. H. Gerischer and M. Lübke, *Ber. Bunsenges. phys. Chem.* **92**, 573 (1988).
89. J. Stumper and L. M. Peter, *J. electroanal. Chem.*, in press.
90. H. Jungblut, private communication.